
**1 Revisiting the Austral Spring Extratropical Southern
2 Hemisphere zonally assymetric circulation using
3 complex Empirical Orthogonal Functions**

**4 Elio Campitelli · Leandro B. Díaz ·
5 Carolina Vera ·**

6
7 Received: date / Accepted: date

8 Abstract abstract

9

10 Keywords ·

The research was supported by UBACyT20020170100428BA and the CLIMAX Project funded by Belmont Forum/ANR-15-JCL/-0002-01. Elio Campitelli was supported by a PhD grant from CONICET, Argentina.

Elio Campitelli
Universidad de Buenos Aires, Facultad de Ciencias Exactas y Naturales, Departamento de Ciencias de la Atmósfera y los Océanos. Buenos Aires, Argentina.
CONICET – Universidad de Buenos Aires. Centro de Investigaciones del Mar y la Atmósfera (CIMA). Buenos Aires, Argentina.
CNRS – IRD – CONICET – UBA. Instituto Franco-Argentino para el Estudio del Clima y sus Impactos (IRL 3351 IFAECI). Buenos Aires, Argentina.
E-mail: elio.campitelli@cima.fcen.uba.ar

Leandro B. Díaz
Universidad de Buenos Aires, Facultad de Ciencias Exactas y Naturales, Departamento de Ciencias de la Atmósfera y los Océanos. Buenos Aires, Argentina. CONICET – Universidad de Buenos Aires. Centro de Investigaciones del Mar y la Atmósfera (CIMA). Buenos Aires, Argentina. CNRS – IRD – CONICET – UBA. Instituto Franco-Argentino para el Estudio del Clima y sus Impactos (IRL 3351 IFAECI). Buenos Aires, Argentina.

Carolina Vera
Universidad de Buenos Aires, Facultad de Ciencias Exactas y Naturales, Departamento de Ciencias de la Atmósfera y los Océanos. Buenos Aires, Argentina. CONICET – Universidad de Buenos Aires. Centro de Investigaciones del Mar y la Atmósfera (CIMA). Buenos Aires, Argentina. CNRS – IRD – CONICET – UBA. Instituto Franco-Argentino para el Estudio del Clima y sus Impactos (IRL 3351 IFAECI). Buenos Aires, Argentina.

11 1 Introduction**introduction**

12 The large-scale extratropical circulation in the Southern Hemisphere is strongly
13 zonally symmetric, but its zonal departures are highly relevant for surface im-
14 pacts and could be related to high-impact climate extremes. Zonal asymme-
15 tries of extratropical circulation in the Southern Hemisphere strongly modulate
16 weather systems and regional climate through latitudinal transport of heat,
17 humidity, and momentum (Trenberth, 1980).

18 One of the main features of the zonally asymmetric circulation are the
19 Pacific–South American Patterns (Mo and Paegle, 2001), which are associ-
20 ated with precipitation anomalies in South America. Besides, Raphael (2007)
21 suggests that variability in the planetary wave 3 projected onto its climato-
22 logical location is associated with Antarctic sea ice concentration anomalies.
23 Irving and Simmonds (2015) showed that planetary wave amplitude in general
24 is associated sea ice concentration, as well as temperature and precipitation
25 anomalies.

26 Some of these patterns of variability associated to the zonally asymmet-
27 ric circulation appear to have experienced secular changes, although to our
28 knowledge this has not been extensively studied. For instance, Raphael (2003)
29 found that the amplitude of the zonal wave 1 experienced a large increase and
30 that the zonal wave 3 experienced changes in its annual cycle between 1958
31 and 1996.

32 One typical way of describing the zonally asymmetric circulation is by
33 the amplitude and phase of zonal waves obtained by Fourier decomposition
34 of geopotential height at each latitude (e.g. van Loon and Jenne, 1972; Tren-
35 berth, 1980; Turner et al, 2017). This approach suggests that zonal waves 1 and
36 3 explained most of the variance of the tropospheric extratropical Southern
37 Hemisphere circulation (van Loon and Jenne (1972)). However, this method-
38 ology relies on the assumption that the circulation can be meaningfully un-
39 derstood in terms of zonal waves of constant amplitude along a latitude circle.
40 This is not valid for meridionally propagating waves or zonal waves with lo-
41 calised amplitudes. In the case of the wave 3, for example, Trenberth and Mo
42 (1985) observed that it played a role in blocking events, but this was mostly
43 due to increased amplitude of a longitudinally localised wave train instead of
44 an hemispheric-scale zonal wave 3.

45 The fourier technique can be generalised to integrate all planetary wave in-
46 tensity irregardless of wave number by computing the wave envelope as done
47 by Irving and Simmonds (2015). This makes it possible to represent plane-
48 tary waves with different amplitude at different longitudes, but it removes all
49 information about phase and wave number.

50 Another approach to characterising the Southern Hemisphere circulation is
51 by using Empirical Orthogonal Functions (EOF, also known as Principal Com-
52 ponent Analysis). Within the EOF framework, the Southern Annular Mode
53 (SAM) appears as the leading mode of variability of the tropospheric South-
54 ern Hemisphere circulation (Fogt and Marshall, 2020) followed by the two
55 PSA (Mo and Paegle, 2001). The SAM represents a relatively zonally sym-

metric pattern of alternating low pressures in polar latitude and a ring of high pressures in high latitudes with an embedded wave 3 pattern that is more prominent in the Pacific sector. The PSA1 and PSA2 describe the two out-of-phase sides of a meridionally propagating wave train that originates in the Eastern equatorial Pacific and travels towards the South Atlantic following a great-circle arch along the Antarctic Peninsula. These patterns are derived by applying EOF to temporal anomalies, but Raphael (2003) applied EOF methods specifically to zonal anomalies.

EOFs are more flexible than Fourier decomposition modes in the sense that they can capture oscillation patterns that cannot be characterised by purely sinusoidal waves with constant amplitude. Nonetheless, they are restricted to standing oscillation modes and could not represent properly propagating or phase-varying modes such as zonal waves. A single EOF can also represent a mixture of two or more physical modes. The inability of a single EOF to describe travelling waves is what forces the PSA pattern to be described by two EOFs. Irving and Simmonds (2016) characterises this pattern in a Fourier framework. Being a meridionally propagating mode, the PSA cannot be correctly characterised by Fourier decomposition at each latitude circle. As a result, they reprojected meridional wind fields so that the path of the PSA laid on the equator. On this new projection, they could identify the PSA using Fourier decomposition.

Finally, another, hybrid, methodology commonly used consist on identifying particular features of interest and creating indices using simple methods such as averages and differences. The Marshal SAM Index (Marshall, 2003), for example, tries to characterise the SAM by the average difference of sea level pressure between 40°S and 65°S, following Gong and Wang (1999). Raphael (2004) used a similar methodology to describe the wave 3 in the Southern Hemisphere. Instead of using Fourier to compute the amplitude and phase of the zonal wave, they averaged standardised geopotential height anomalies in three points representing the location of the ridges of the zonal wave 3 of the climatological mean. This is equivalent to an index of the amplitude of the zonal wave 3 that projects into the phase of the zonal wave 3 of the mean field. Similarly, Hobbs and Raphael (2010) propose that the zonally asymmetric circulation in the Southern Hemisphere can be described by the strength and location of two anticyclones located in the sub-Antarctic western hemisphere. These methods are grounded on other methods to identify the centres of action for the described phenomena and can be useful to characterise features that are not readily apparent with Fourier or EOF methods. The use of data of only specific regions or locations makes them suitable for easy computation and for extending back into the data-poor past, but also makes them not very robust and unable to capture non-stationary patterns.

Our objective is to improve our understanding of planetary waves in the Southern Hemisphere using an index that is able to capture the phase-varying nature of planetary waves and is flexible enough to describe planetary waves with non-constant amplitude in each latitude circle. We use complex Empirical Orthogonal Functions (Horel, 1984) as a robust extension of EOF analysis that

102 is capable of describing rich structures with meridional and zonal propagation,
 103 and amplitude modulation such as the PSA.

104 We apply this method to characterise the Springtime zonally asymmetric
 105 circulation of the extratropical Southern Hemisphere. To take vertical distri-
 106 bution into account, we analyse both the troposphere and the stratosphere.
 107 We focus the analysis to the September-October-November because that's the
 108 trimester in which tropical forcing of zonal waves is maximised (cita). **Este**
 109 **parráfo me parece que quedo un poco colgado. Creo que sería importante que**
 110 **esté desde más arriba la idea de la primavera, ya que todo lo otro es muy**
 111 **general, pero al final el análisis solo se va a restringir a esta estación**

112 In Section 2 we describe the methods. In Section 3.1, we analyse the spatial
 113 patterns of each complex EOF. In Section 3.2 we study the spatial regressions
 114 with geopotential height and temperature. In Section 3.3, we analyse the rel-
 115ationship between cEOF1 and Ozone, and between EOF2 and the Southern
 116 Annular Mode and the PSA. In Section 3.4 we look for tropical forcings that
 117 explain the variability of each cEOF. Finally, in Section 3.5 we show the rela-
 118tionship between these modes of variability and precipitation in South America
 119 and Oceania.

120 2 Data and Methods

121 2.1 Data

122 We used monthly geopotential height, air temperature, ozone mixing ratio,
 123 and total ozone column (TOC) at 2.5° longitude by 2.5° latitude of hori-
 124zontal resolution and 37 vertical isobaric levels from the European Centre
 125 for Medium-Range Weather Forecasts Reanalysis version 5 [ERA; Hersbach
 126 et al (2019)] for the period 1979-2019. Most of our analysis was restricted to
 127 the post-satellite era to avoid any confounding factors arising from the in-
 128corporation of satellite observations, but we also used the preliminary back
 129 extension of ERA5 from 1950 to 1978 (Bell et al, 2020) to look at long-term
 130 trends. Streamfunction was derived from ERA5 vorticity at 200 hPa using the
 131 FORTRAN subroutine FISHPACK (Adams et al, 1999) and horizontal wave
 132 activity fluxes was computed following Plumb (1985). We used Sea Surface
 133 Temperature (SST) monthly fields from Extended Reconstructed Sea Surface
 134 Temperature (ERSST) v5 (Huang et al, 2017) and precipitation monthly data
 135 from the CPC Merged Analysis of Precipitation (Xie and Arkin, 1997), with a
 136 2.5° resolution in latitude and longitude. This rainfall gridded dataset is based
 137 on information from different sources such as rain gauge observations, satellite
 138 inferred estimations and the NCEP-NCAR reanalysis, and it is available since
 139 1979 to present.

140 2.2 Methods

methods-1

141 The study is restricted to the spring season, defined as the September-October-
142 November (SON) trimester. We compute seasonal means for the different vari-
143 ables, averaging monthly values weighted by the number of days in each month.
144 We use 200 hPa level to represent the high troposphere and 50 hPa to represent
145 the lower stratosphere.

146 The amplitude of the zonal waves was obtained through the Fourier trans-
147 form of the spatial field at each latitude circle. We computed the amplitude
148 and phase of the zonal wave 1 by averaging (area-weighted) each variable be-
149 tween 75°S and 45°S for each SON and extracting the wave-1 component of
150 the Fourier spectrum. We chose this latitude band because it is wide enough to
151 capture most of the relevant anomalies for southern hemisphere mid-latitudes.

152 We computed the level-dependent SAM index as the leading EOF of year-
153 round monthly geopotential height anomalies south of 20°S at each level for the
154 whole period according to Baldwin and Thompson (2009). We further split the
155 SAM into its zonally symmetric and zonally asymmetric components (S-SAM
156 and A-SAM indices respectively). These indices were obtained by projecting
157 the zonally asymmetric and zonally symmetric part of the SAM spatial pattern
158 onto monthly geopotential height fields, as proposed by Campitelli et al (2021).
159 Seasonal indices of the Pacific South American patterns (PSA1 and PSA2)
160 were calculated following Mo and Paegle (2001) as the third and fourth leading
161 EOF of seasonal mean anomalies for SH 500 hPa geopotential height combining
162 all seasons. In our study, only the SON values were used.

163 Linear trends were computed by Ordinary Least Squares (OLS) and the
164 95% confidence interval was computed assuming a t-distribution with the ap-
165 propriate residual degrees of freedom (Wilks, 2011).

166 2.3 Complex Empirical Orthogonal Functions (cEOF)

complex-empirical-orthogonal-functions-ceof

167 **En la figura 1 te quedaron muy chicos los subplots, amplialos un poco.**

168 In traditional EOF analysis zonal waves appear as pairs of EOFs, that
169 could be degenerated representing similar patterns but shifted in phase (Horel,
170 1984). For instance, Figure 1 shows the leading 4 EOFs of SON geopotential
171 height zonal anomalies at 50 hPa south of 20°S. It is clear that the first two
172 EOFs represent the same zonal wave 1 pattern and the last two represent a
173 same zonal wave pattern with shorter wavenumber and four centers of action
174 shifted by 1/4 wavelength. A similar EOF structure can be seen in 200 hPa
175 (not shown). Since each pair of EOFs seem to represent the same phase-varying
176 structure, it would be desirable to combine them into a single index with
177 amplitude and phase.

178 Complex Empirical Orthogonal Functions (cEOF) is a useful method to
179 characterise zonal waves, considering phase-varying structures (Horel, 1984).
180 This method involves computing EOF on the analytic representation of the
181 original field. This representation is a complex field in which the real part is the

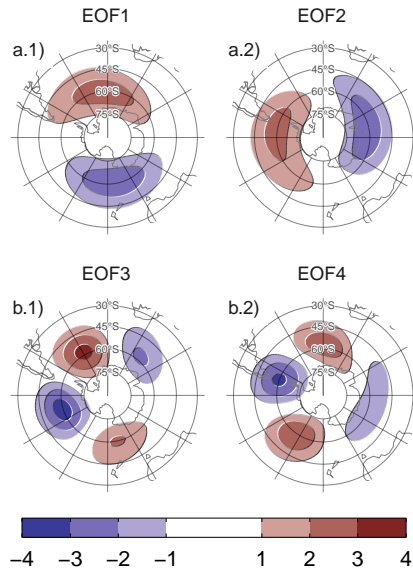


fig:eof-naive
Fig. 1: Spatial patterns of the leading 4 EOFs of SON zonal anomalies of geopotential height at 50 hPa south of 20°S for the 1979 – 2019 period (arbitrary units).

182 original variable and the imaginary part is the original data shifted by 90° at
 183 each spectral frequency – i.e. its Hilbert transform. The Hilbert transform is
 184 usually understood in terms of time-varying signal. However, in this work we
 185 apply the Hilbert transform to each latitude circle at each moment in time.
 186 Since each latitude circle is a periodic domain, this procedure does not suffer
 187 from edge effects.

188 The result of the cEOF methodology is a set of complex spatial patterns
 189 and complex time series. The real and imaginary part of each spatial pattern
 190 represent two phases wave-like spatial patterns that are in quadrature. The
 191 magnitude and argument of each complex time series represent the amplitude
 192 and phase of each zonal wave.

193 *Los colores de la Tabla 1 no dicen mucho en la medida que no se conoce
 194 cuál sería la paleta. Quizás se pueden remarcar en negrita ambos aclarando
 195 que son significativos (lo son?).*

196 The cEOF methodology is applied to SON geopotential height zonal anomalies
 197 south of 20°S at 50 and 200 hPa, representing a stratospheric and upper
 198 tropospheric level respectively. Table 1 shows the coefficient of determination
 199 between time series of the amplitude of each complex EOF (cEOF) across
 200 levels. There's a high degree of correlation between the magnitude of the re-
 201 spective cEOF1 and cEOF2 at each level. The spatial patterns of the 50 hPa
 202 and 200 hPa cEOFs are also similar (not shown).

203 Both the spatial pattern similarity and the high temporal correlation of
 204 cEOFs computed at 50 hPa and 200 hPa suggest that these are, to a large

tab:corr-ceof-splitted
Table 1: Coefficient of determination (R^2) of the absolute magnitude of complex EOFs between 200 hPa and 50 hPa computing EOF separately for each level. Background colour indicates the value of R^2 .

		50 hPa		
200 hPa		cEOF1	cEOF2	cEOF3
cEOF1	0.28	0.01	0.02	
cEOF2	0.00	0.60	0.02	
cEOF3	0.00	0.00	0.02	

205 extent, modes of joint variability. This motivates the decision of performing
 206 complex EOF jointly between levels. The computation of the cEOFs was car-
 207 ried out using data from both levels at the same time, therefore, each cEOF
 208 has a spatial component that depends on longitude, latitude and level, and a
 209 temporal component that depends only on time.

210 The phase of principal components is defined up to an additive constant.
 211 For real principal components, this constant can be either 0 or π , correspond-
 212 ing to a change in sign. For complex principal components, it can be any
 213 number between 0 and 2π (Horel, 1984). Since any choice is arbitrary and
 214 equally valid, we chose the phase of each cEOF so that the real and imaginary
 215 parts are aligned with meaningful phases in our analysis. This procedure does
 216 not create a spurious correlation, it only takes a known relationship and aligns
 217 it with a specific phase. For the first complex principal component, the phase
 218 was chosen so that the time series corresponding to the real part has the max-
 219 imum correlation with the zonal wave 1 of Total Ozone Column between 75°S
 220 and 45°S. This also nearly minimises the correlation with the imaginary part.
 221 For the second complex principal component, the phase was chosen so that
 222 the coefficient of determination between the Oceanic Niño Index (Bamston
 223 et al, 1997) and the real part was minimized, which also nearly maximizes the
 224 correlation with the imaginary part.

225 While we compute these complex principal components using data from
 226 1979 to 2019, we extended the complex time series back to the 1950 – 1978
 227 period by projecting monthly geopotential height zonal anomalies standardised
 228 by level south of 20°S onto the corresponding spatial patterns.

229 We performed linear regressions to quantify the association between the
 230 cEOFs and other variables. For each cEOF, we create regression maps by
 231 fitting a multiple linear model involving both the real and the imaginary part.
 232 To obtain the linear coefficients of a variable X (geopotential, temperature,
 233 precipitation, etc...) with the Imaginary and Real parts of each cEOF we fit
 234 the equation

$$X(\lambda, \phi, t) = \alpha(\lambda, \phi) \operatorname{Im}(\text{cEOF}) + \beta(\lambda, \phi) \operatorname{Re}(\text{cEOF}) + X_0(\lambda, \phi) + \epsilon(\lambda, \phi, t)$$

235 where λ and ϕ are the longitude and latitude, t is the time, α and β are
 236 the linear regression coefficients for Imaginary and Real parts respectively, X_0
 237 and ϵ are the constant and error terms respectively.

238 We evaluated statistical significance using a two-sided t-test and, in the
 239 case of regression maps, p-values were adjusted by controlling for the False
 240 Discovery Rate (Benjamini and Hochberg, 1995; Wilks, 2016) to avoid mis-
 241 leading results from the high number of regressions (Walker, 1914; Katz and
 242 Brown, 1991).

243 2.4 Computation procedures

244 We performed all analysis in this paper using the R programming language
 245 (R Core Team, 2020), using data.table (Dowle and Srinivasan, 2020) and
 246 metR (Campitelli, 2020) packages. All graphics are made using ggplot2 (Wick-
 247 ham, 2009). We downloaded data from reanalysis using the ecmwfr package
 248 (Hufkens, 2020) and indices of the ENSO with the rsoi package (Albers and
 249 Campitelli, 2020). The paper was rendered using knitr and rmarkdown (Xie,
 250 2015; Allaire et al, 2020).

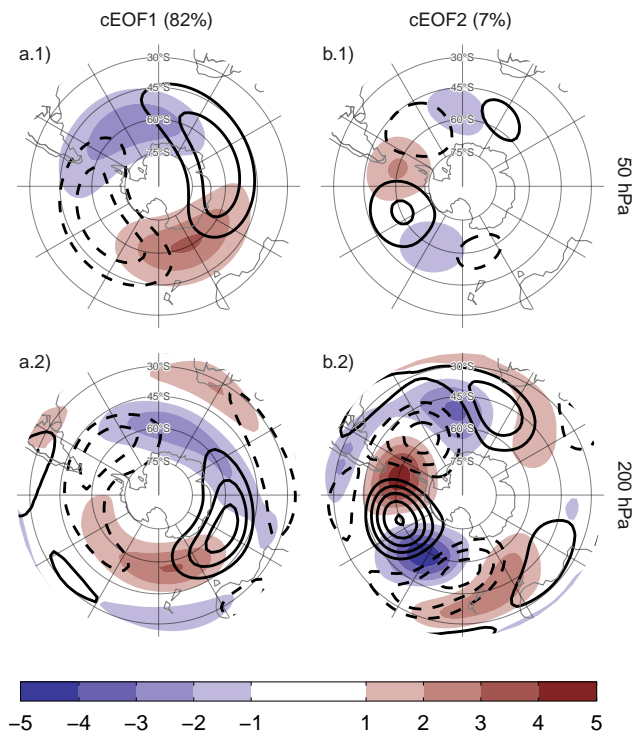
251 3 Results

252 3.1 cEOF spatial patterns

253 To describe the variability of the circulation zonal anomalies, the spatial and
 254 temporal parts of the first two leading cEOFs of zonal anomalies of geopotential
 255 height at 50 hPa and 200 hPa, computed jointly at both levels, are shown in
 256 Figures 2 and 3. The first mode (cEOF1) explains 82% of the variance, while
 257 the second mode (cEOF2) explains a smaller fraction (7%). In the spatial
 258 patterns (Fig. 2), the real and the imaginary components are in quadrature
 259 by construction, so that each cEOF describe a single wave-like pattern whose
 260 amplitude and position (i.e. phase) is controlled by the magnitude and phase
 261 of the temporal cEOF. The wave patterns described by these cEOFs match
 262 the patterns seen in the traditional EOFs of Figure 1.

263 tengo la impresión de que en la figura 2 podría estar un poco más grandes
 264 los subplots para se vean más fácilmente los detalles

265 The cEOF1 (Fig. 2 column a) is a hemispheric wave 1 pattern with maxi-
 266 mum amplitude at high latitudes. At 50 hPa the Real cEOF1 has the maximum
 267 of the wave 1 at 150°E and at 200 hPa, the maximum is located at around
 268 175°E indicating a westerly shift in phase. The cEOF2 (Fig. 1 column b) shows
 269 also a zonal wave-like structure with maximum amplitude at high latitudes,
 270 but with shorter spatial scales. In particular, its dominant structure at both
 271 levels is a wave 3 but with larger amplitude in the pacific sector. This modu-
 272 lated amplitude is especially apparent at 200 hPa. There is no apparent phase
 273 shift but the amplitude of the pattern is greatly reduced in the stratosphere,



^{fig:ceofs-1}
Fig. 2: Spatial patterns for the two leading cEOFs of SON zonal anomalies of geopotential height at 50 hPa and 200 hPa for the 1979 – 2019 period. The shading (contours) corresponds to real (imaginary) part. Arbitrary units.

274 suggesting that this barotropic mode represents mainly tropospheric variability.
275

276 se me vino una duda, ¿se pueden comparar de algún modo las amplitudes
277 que mostras en esta figura? en caso de que si, creo que habría que mencionar
278 algo sobre lo que pasa con el cEOF2 en la estratosfera All cEOFs have non
279 zero mean (Fig. 3) because the geopotential fields that enter into the cE-
280 OFs algorithm are anomalies with respect to the zonal mean instead of the
281 time mean. However, cEOF2's mean is almost zero, which indicates that only
282 cEOF1 includes variability that significantly projects onto the mean zonally
283 anomalous field. There are no significant simultaneous correlation between the
284 time series. Both cEOFs show year-to-year variability but show no evidence of
285 decadal variability.

286 En la figura 3 agregaría dos cosas: i)el eje y en la columna derecha (si la
287 queres ver más grande perdes la referencia) ii) creo que serviría agregar una
288 líneas verticales en la grilla para poder tener una idea un poco mejor de a
289 qué años corresponde más o menos cada valor. pueden ser un poco más finas
290 que las que ya están, pero creo que sería una referencia util para visualmente

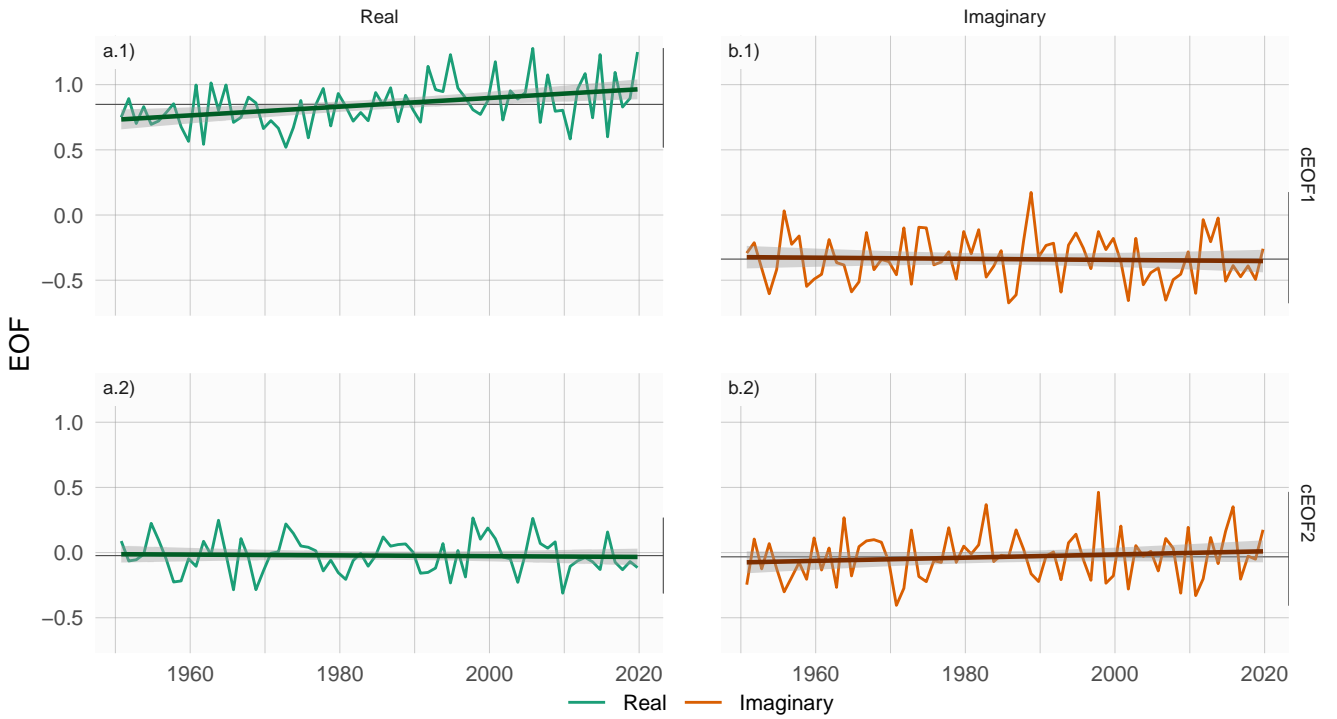


Fig. 3: Time series extended using ERA5 back extended preliminary edition (period 1950 – 1978) and ERA5 (period 1979 – 2019). Dark straight line is the OLS trend. Black horizontal and vertical line mark the mean value and range of each time series respectively.

`fig:extended-series`

291 poder decir a qué año corresponde cada punto. Además, fijate que la figura te
 292 quedo de un ancho mayor que el de la página y te quedo un "EOF" en el eje-y
 293 a la izquierda que no creo que sea lo más correcto.

294 There is only a significant upward trend in the real component of cEOF1
 295 (Fig. 3a.1, p-value < 0.001) and no significant trend in any of the complex
 296 components of cEOF2. The positive trend in the Real cEOF1 translates into
 297 a positive trend in cEOF1 magnitude, but not in the phase (not shown). This
 298 long-term change indicates an increase in the magnitude of the high latitude
 299 zonal wave 1. A similar observation was made by Raphael (2003), who detected
 300 a step after around 1975 in the leading EOF of August-September-October 500
 301 hPa zonal geopotential height anomalies, which is similar to the cEOF1.

302 3.2 cEOFs Regressions

303 The spatial patterns shown in Figure 2 are derived by removing the zonally
 304 symmetric circulation, so they might not include all the variability that is actu-

`regressions`

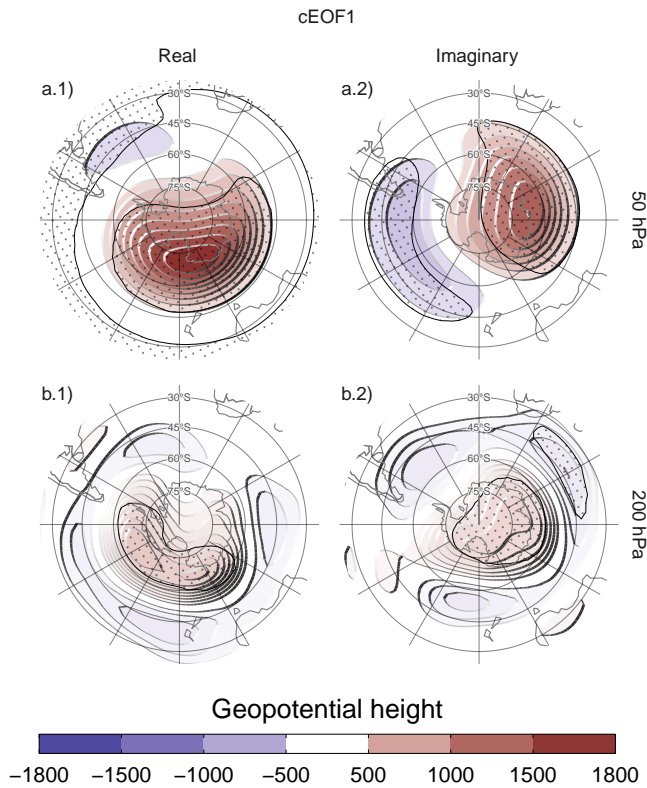


fig: eof1-regr-gh
 Fig. 4: Regression of SON geopotential height anomalies (meters) with the (column 1) real and (column 2) imaginary parts of the first cEOF for the 1979 – 2019 period at (row a) 50 hPa and (row b) 200 hPa. These coefficients come from multiple linear regression involving the real and imaginary parts. Areas marked with dots have p-values smaller than 0.05 adjusted for False Detection Rate.

305 ally associated with the cEOF time series. To understand the full geopotential
 306 height field changes associated with each cEOF, we computed regression pat-
 307 terns of the full geopotential fields onto each cEOF.

308 Figure 4 shows regression maps of SON geopotential height anomalies upon
 309 cEOF1. At 50 hPa (Figure 4 row a), both the Real and Imaginary cEOF1 are
 310 associated with planetary wave 1 patterns, that are 90° out of phase. Their
 311 phases coincide with the ones shown in Figure 2a.1, with the positive centre
 312 of the Real cEOF1 located towards the dateline, and the one of the Imaginary
 313 cEOF1 located over Eastern Antarctica. However, the Real cEOF1 pattern is
 314 substantially altered by the zonally symmetric circulation. Instead of a clear
 315 wave 1 pattern, the regression pattern can be better described as a monopole
 316 with its centre displaced from the South Pole.

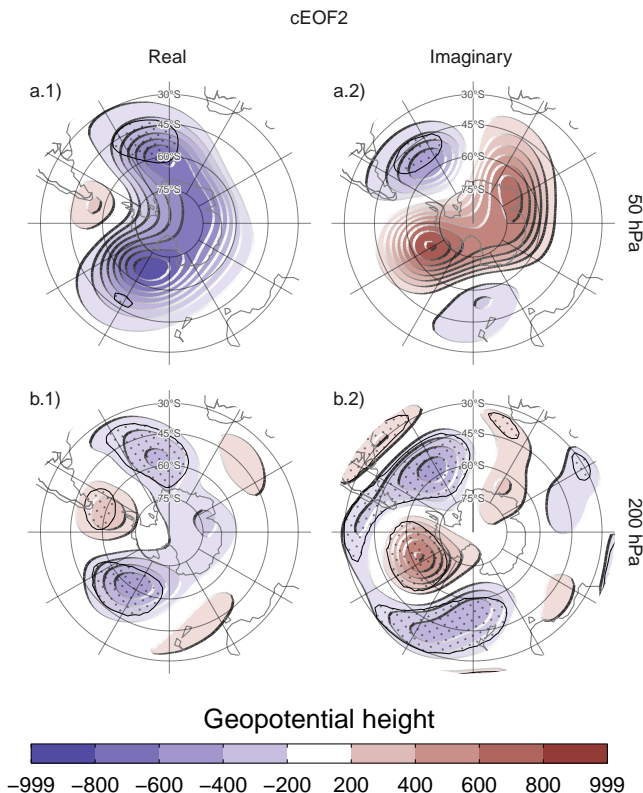


Fig. 5: ^{fig: eof2-regr-gh} Same as Figure 4 but for the second cEOF.

317 La figura 4 la veo muy saturada con los puntos que indican la significan-
 318 cia. ¿se podrá hacer con un tamaño menor? ¿Las unidades son correctas?
 319 Me llama la atención que te puedan dar tantos cientos de metros de altura
 320 geopotencial.

321 The regression patterns for cEOF1 at 200 hPa (Figure 4 row b) are sim-
 322 ilarly influenced by the zonally symmetric circulation. It is only possible to
 323 partially distinguish the wave 1 pattern in relation with the Real cEOF1 (Fig-
 324 ure 4b.1). The Imaginary cEOF1 shows a much more zonally symmetrical
 325 pattern resembling the negative SAM phase.

326 With the exception of the Imaginary cEOF1, it is clear that these patterns
 327 are very different than the fully zonally asymmetric versions (Fig. 2), partic-
 328 ularly at 200 hPa. Moreover, only in the stratosphere these patterns actually
 329 show a distinguishable wave 1 pattern shifted in phase by 90°, suggesting that
 330 using the cEOF method is artificially generating a wave structure at 200hPa.
 331 Therefore, the magnitude and phase of the cEOF1 are associated with the
 332 magnitude and phase of a zonal wave only in the stratosphere. While in the
 333 troposphere, they are associated with slightly off-centre monopoles.

334 Figure 5 shows the regression pattern of geopotential height anomalies
335 upon the cEOF2. Unlike for cEOF1, in this case the regression patterns are
336 similar to the fully zonally asymmetric patterns from Figure 2. Although there
337 are some differences (particularly in 50 hPa), the wave trains identified before
338 are well characterised and patterns associated with the Real cEOF2 are 90°
339 out of phase with those associated with the Imaginary cEOF2. Zonal wave
340 3 dominates all fields, but only in the western hemisphere, over the Pacific
341 and Atlantic Oceans. cEOF2 then represents an equivalent barotropic wave
342 train that is very similar to the the Pacific South American Patterns (Mo and
343 Paegle, 2001). Comparing the location of the positive anomaly near 90°W in
344 column b of Figure 5 with Figures 1.a and b from Mo and Paegle (2001), the
345 Real cEOF2 can roughly be identified with PSA2, while the Imaginary cEOF2
346 resembles PSA1.

347 Figura 5. Me resulto raro que vaya hasta 999 en vez de 1000

348 3.3 cEOFs relationship with known modes of variability

other-variables

349 3.3.1 SAM

sam

350 To explore the relationship between SAM and the modes described from the
351 cEOF, we compute the coefficient of determination between the cEOFs time-
352 series and the three SAM indices (SAM, A-SAM and S-SAM) at each ver-
353 tical level (Fig. 6). The SAM index is statistically significant correlated with
354 the Real cEOF1 in all levels, and with the Imaginary cEOF1 and Imaginary
355 cEOF2 in the troposphere. Correlations between SAM and the Real cEOF2
356 are non-significant.

357 Fig. 6. Te quedan muy pegados los subplots de la columna izquierda con
358 los de la derecha. Recomendaría aumentar el espacio intermedio y repetir el
359 eje y en las figuras de la derecha. Además podrías agregar el y-label (Level) a
360 la izquierda.

361 The relationship between the tropospheric SAM and cEOF1 is explained
362 entirely by the zonally symmetric component of the SAM as shown by the low
363 and statistically non-significant correlations between the A-SAM and either
364 the Real or Imaginary cEOF1 and the high correlation with the S-SAM below
365 100 hPa. In the stratosphere, the Real cEOF1 is correlated with both A-
366 SAM and S-SAM, while the Imaginary cEOF1 is highly correlated only with
367 the A-SAM. These correlations are consistent with the regression patterns of
368 geopotential height in Figure 4 and their comparison with those obtained for
369 SAM, A-SAM and S-SAM by Campitelli et al (2021).

370 In the case of cEOF2, the moderate correlation between SAM and Imag-
371 inary cEOF2 becomes extremely high only when the zonally asymmetric vari-
372 ability of the SAM is considered. The Imaginary cEOF2 explains up to 92% of
373 A-SAM variance, reached the maximum value at 225 hPa (Figure 6.b2). Such
374 extremely high correlation between the asymmetric SAM and the Imaginary

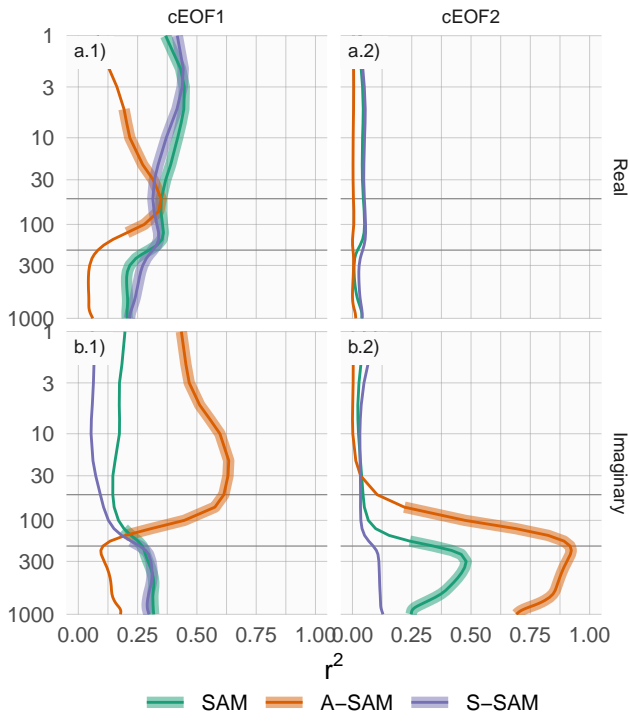


Fig. 6: Coefficient of determination between the real and imaginary part of each cEOF and the SAM, Asymmetric SAM (A-SAM) and Symmetric SAM (S-SAM) indices computed at each level according to Campitelli et al (2021). Thick lines represent estimates with p -value < 0.01 corrected for False Detection Rate (Benjamini and Hochberg, 1995).

375 cEOF2 suggests that these might be different ways of characterising the same
376 phenomenon.

377 *3.3.2 PSA*

378 *Tabla 2. Mismo comentario que antes con lo del background color (no dice
379 mucho si no se conoce la escala), quizás podes destacar en negritas seg\xfcrea la
380 significancia. ¿Está bien el intervalo de confianza de PSA2 vs cEOF2 Im? Hay
381 algo raro ah\xed*

382 Due to the similarity between the PSA patterns and the cEOF2 spatial
383 patterns (Fig. 5), we study the relationship between these modes. Table 2
384 shows the correlations between the two PSA indices and the timeseries for Real
385 and Imaginary phase of cEOF2. As anticipated by Figure 5, there is a strong
386 correlation between PSA1 and Imaginary cEOF2, and between PSA2 and Real
387 cEOF2. Conversely, there is no relationship between PSA1 and Real cEOF2,
388 and between PSA2 and Imaginary cEOF2. As a result, cEOF2 represents well

Table 2: Correlations between the Real and Imaginary parts of cEOF2 and the PSA1 and PSA2 modes computed as the second and third EOFs of seasonal geopotential height anomalies (following Mo and Paegle, 2001) for the 1979 – 2019 period. 95% confidence intervals in parenthesis. Background colour indicates the value of correlation.

PC	cEOF2	
	Real	Imaginary
PSA1	-0.32 (CI: -0.57 – -0.015)	-0.82 (CI: -0.9 – -0.69)
PSA2	0.81 (CI: 0.67 – 0.9)	-0.062 (CI: -0.36 – 0.25)

389 both the spatial structure and temporal evolution of the PSA modes, as well
 390 as it is possible to make a rather clean association between its two phases
 391 and the two PSA modes. So, It could be concluded that the same particular
 392 rotation of cEOF2 that maximises the association between cEOF2 parts and
 393 PSA modes, is the one which maximises the relationship between ENSO and
 394 Imaginary cEOF2.

395 The reason the conventional EOF analysis arrives at the same separation
 396 than our particular cEOF rotation is probably the fact that not all phases are
 397 equally frequent. To visualize that, Figure 7 shows an histogram that counts
 398 the number of SON years in which the cEOF2 was close to each of the four
 399 particular phases (positive/negative Real/Imaginary), with the observations
 400 for each season marked as rugs on the horizontal axis. For instance, years
 401 with cEOF2 phase within 45° of 0° are nearest the “positive Real” phase.
 402 About two thirds of time cEOF2 has a phase similar to either the negative
 403 or positive Imaginary phase. It could be seen that Imaginary phase is the
 404 most common phase and It is also, by construction, the direction that has the
 405 maximum relationship with ENSO. Therefore, the Imaginary cEOF2 explains
 406 more variance than the Real cEOF2 and conventional EOF analysis will tend
 407 to separate the two.

408 The result obtained here is similar to the one obtained by Irving and Sim-
 409 monds (2016). They show that the phase distribution of the PSA-like variabil-
 410 ity obtained by them is bimodal and isolate the PSA pattern from the rest
 411 of the PSA-like variability by selecting events that are near the peaks of the
 412 distribution (compare our Figure 7 with their Figure 6).

413 The advantage of our method is that it is much simpler to implement,
 414 it provides magnitude and phase naturally, and it facilitates the description
 415 of this mode as a propagating wave instead of as standing oscillations. As a
 416 consequence, the cEOF2 offers an alternative way of representing the PSA
 417 which has several advantages over using the second and third EOFs.

418 3.3.3 Temperature and Ozone

temperature-and-ozone

419 The relation between cEOFs and air temperature was also evaluated. Fig-
 420 ure 8 shows regression patterns of air temperature at 50hPa and 200hPa onto

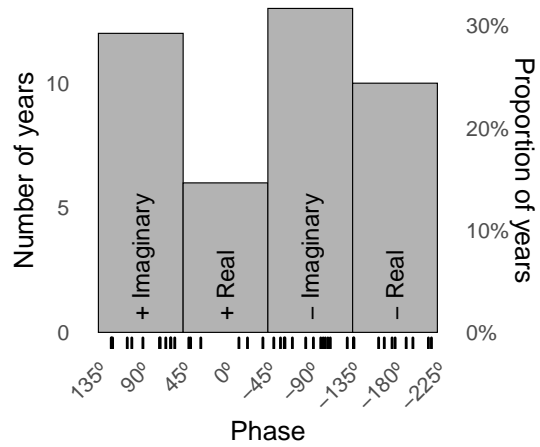


Fig. 7: `fig:phase-histogram` Histogram of phase distribution of cEOF2 for the 1979 – 2019 period. Bins are centred at 90° , 0° , -90° , -180° with a binwidth of 90° . The small vertical lines near the horizontal axis mark the observations.

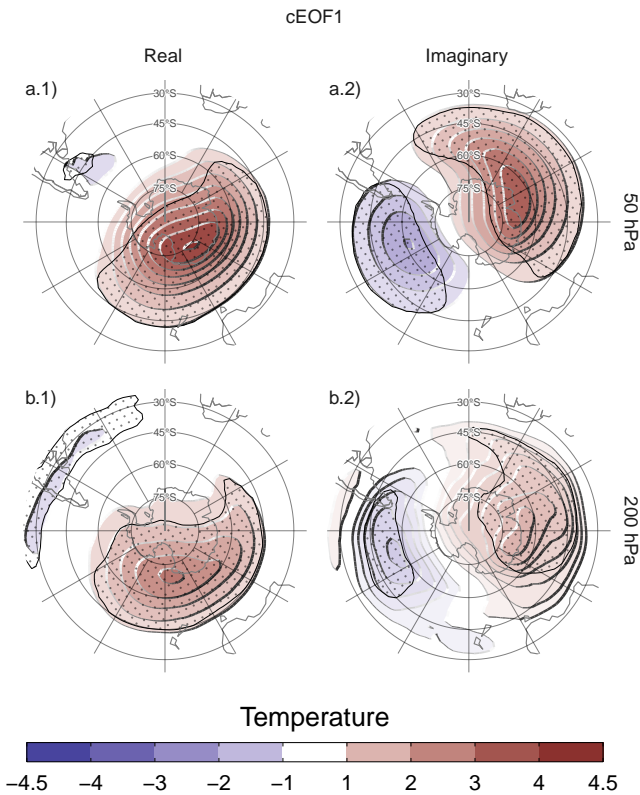


Fig. 8: `fig: eof1-regr-t` Same as Figure 4 but for air temperature (K).

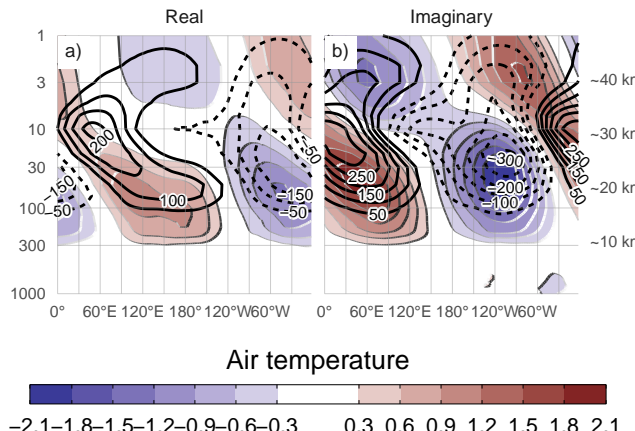


Fig. 9: Regression of SON anomalies of mean air temperature (shaded, Kelvin) and ozone mixing ratio (contours, negative contours with dashed lines, labels in parts per billion by mass) averaged between 75°S and 45°S with the (a) real and (b) imaginary parts of the first cEOF for the 1979 – 2019 period.

421 cEOF1. In both levels, the Real cEOF1 is associated with a positive monopole
 422 over the South Pole with its centre moved slightly towards 150°E (Fig. 8 column 1). On the other hand, the regression maps on the Imaginary cEOF1
 423 show a more clear wave 1 pattern with its maximum around 60°E. The distri-
 424 bution of temperature regression coefficients at 50 hPa and at 200 hPa mirror
 425 the geopotential height regression maps at 50 hPa (Fig. 4).

426 Figure 9 shows the vertical distribution of the regression coefficients on
 427 cEOF1 from zonal anomalies of air temperature and zonal anomalies of ozone
 428 mixing ratio averaged between 75°S and 45°S. Temperature zonal anomalies
 429 associated with cEOF1 show a clear wave 1 pattern for both real and imaginary
 430 components throughout the atmosphere above 250 hPa with a change in sign
 431 above 10 hPa. Following hydrostatic balance, this is the level in which the
 432 geopotential anomaly have maximum amplitude (not shown).

433 The maximum ozone anomalies are co-located with the minimum temper-
 434 ature anomalies above 10 hPa and with the maximum temperature anomalies
 435 below 10 hPa (Fig. 9). Therefore, the ozone zonal wave 1 is anticorrelated
 436 with the temperature zonal wave 1 in the upper stratosphere, and directly
 437 correlated in the upper stratosphere. This change in phase is observed in
 438 ozone anomalies forced by planetary waves that reach the stratosphere. In
 439 the photochemically-dominated upper stratosphere, cold temperatures inhibit
 440 the destruction of ozone. On the other hand, in the advectively-dominated
 441 lower stratosphere, ozone anomalies are 90° out of phase with horizontal and
 442 vertical transport, which are in addition 90° out of phase with temperature
 443 anomalies (Hartmann and Garcia, 1979; Wirth, 1993; Smith, 1995).

444 The regression maps of cEOF1 with fields of Total Ozone Column (TOC)
 445 (Fig. 10) show zonal wave 1 patterns in TOC associated with both phases of

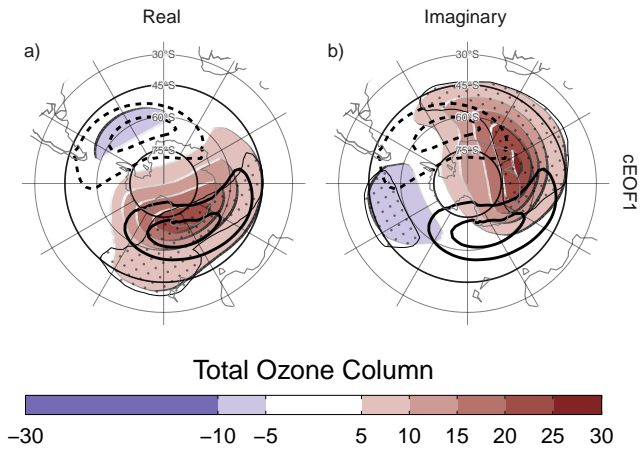


Fig. 10: ^{fig:03-regr} Regression of SON mean Total Ozone Column anomalies (shaded, Dobson Units) with the (a) real and (b) imaginary parts of the cEOF1 for the 1979 – 2019 period. On contours, the mean zonal anomaly of Total Ozone Column (negative contours in dashed lines, Dobson Units). Areas marked with dots have p-values smaller than 0.05 adjusted for False Detection Rate.

447 cEOF1. Climatologically, the springtime Ozone minimum is located off the
 448 South Pole and towards the Weddell Sea (Grytsai, 2011). Thus, the Real
 449 cEOF1 regression pattern (Figure 10a) coincides with the climatological po-
 450 sition of the ozone hole while the one for the Imaginary cEOF1 is shifted by
 451 90°.

452 There is a close spatial relationship between amplitudes and phases of the
 453 cEOF1 and TOC planetary wave 1 between 75°S and 45°S. The correlation
 454 between the amplitude of both indices is 0.77 (CI: 0.61 – 0.87) and 0.49 (CI:
 455 0.21 – 0.69) between their phases.

456 3.4 Tropical sources

457 The connections between cEOFs and Tropical sources are also assessed. Fig-
 458 ure 11 shows the regression maps of Sea Surface Temperatures (SST) and
 459 Streamfunction anomalies at 200 hPa respectively upon cEOF2. The Imagi-
 460 nary cEOF2 is associated with strong positive SST anomalies on the Central
 461 Pacific and negative anomalies over an area across the North of Australia and
 462 New Zealand, the South Pacific Convergence Zone (SPCZ) (Figure 11.a2).
 463 This pattern is almost canonically positive ENSO (Bamston et al, 1997) and
 464 indeed, the correlation between the Imaginary cEOF2 and the Oceanic Niño
 465 Index (Bamston et al, 1997) is significant and very high 0.76 (CI: 0.59 – 0.87).
 466 Besides, the Imaginary cEOF2 is associated with strong wave-like streamfunc-
 467 tion anomalies emanating from the tropics (Figure 11.b2). This is consistent
 468 with the effect of ENSO on the extratropics: SST anomalies initiate anom-

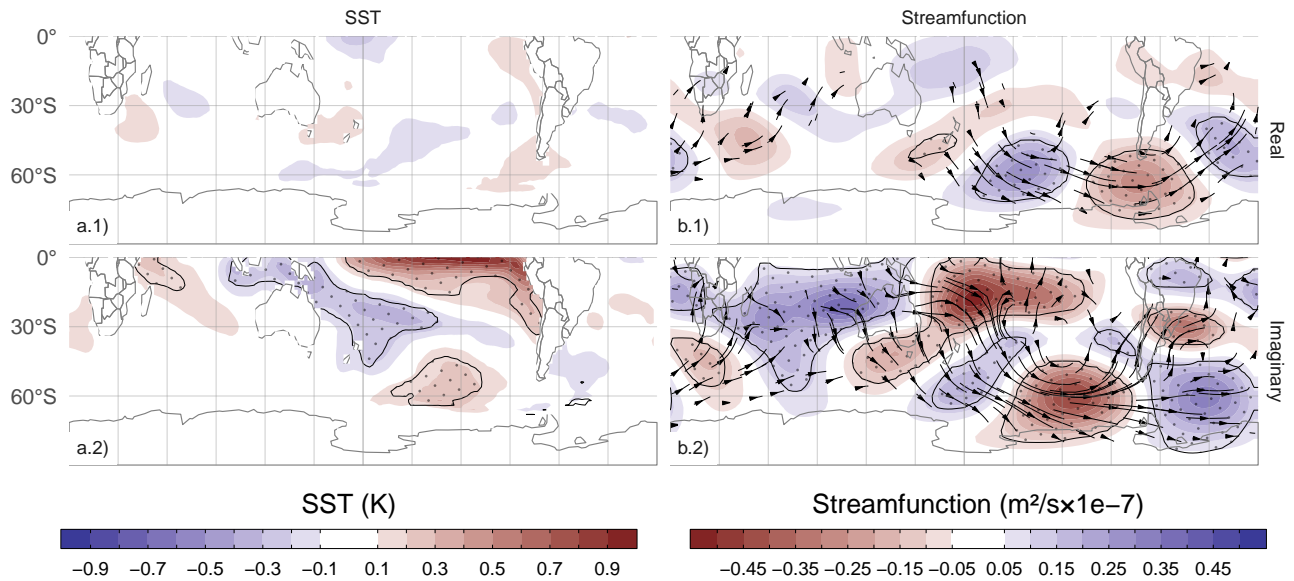


Fig. 11: Regression maps of cEOF2 with SST (K, column a) and streamfunction zonal anomalies ($m^2/s \times 10^{-7}$, shaded) with their corresponding activity wave flux (vectors) (column b). Areas marked with dots have p-values smaller than 0.01 adjusted for FDR.

`fig:sst-psi-2`

469 lous tropical convection that excites Rossby waves that propagate meridionally
 470 towards higher latitudes (Mo, 2000).

471 Since the Real cEOF2 represents just a different phase of the same wave
 472 train, it would be expected to show a similar forcing pattern to the Imaginary
 473 cEOF2 with a slight translation of its location. However, Figure 11.a1 and b1
 474 show that the Real cEOF2 is not associated either with any significant SST
 475 nor streamfunction anomalies in the tropics. The correlation between the Real
 476 cEOF2 and ENSO is also not significant (0.00025 (CI: -0.31 – 0.31)). **Usar**
477 notaci**n** **científica** **por la cantidad de 0 que tiene**. This lack of tropical signal
 478 suggest that the Real cEOF2 and the Imaginary cEOF2 have very different
 479 sources of variability.

480 To better explore the relationship between tropical forcing and phase of the
 481 cEOF2, Figure 12 shows the ONI index against the cEOF2 phase for each SON
 482 trimester between 1979 and 2019, highlighting years in which the magnitude
 483 of cEOF2 is above the median. In years with positive ONI, the phase of the
 484 cEOF2 is mostly around $+90^\circ$ (corresponding with positive imaginary part)
 485 and vice versa. In years with near neutral ENSO, the phase of the cEOF2
 486 is much more variable. The black line in Figure 12 is a sinusoidal fit of the
 487 relationship between ONI and cEOF2 phase. The r^2 corresponding to the fit is
 488 0.56, statistically significant with p-value < 0.001 , indicating a quasi-sinusoidal
 489 relation between these two variables.

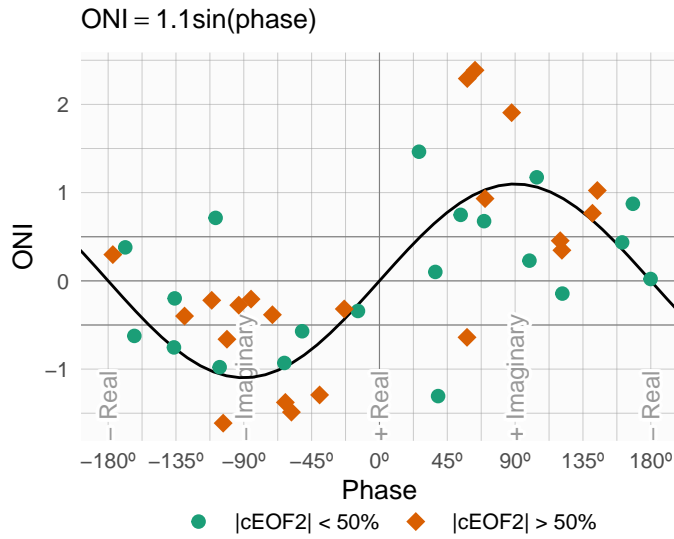


Fig. 12: `fig:enso-phase` ONI plotted against cEOF2 phase for the 1979 – 2019 period. Years with magnitude of cEOF2 greater or smaller than the 50th percentile are shown as orange circles and green diamonds respectively. Black line is the fit $\text{ONI} \sim \sin(\text{phase})$ computed by weighted OLS using the magnitude of the cEOF2 as weights.

490 Fig. 12 Revisa cómo te quedo abajo de la figura la indicación de qué son
 491 cada uno de los puntos (te quedaron dos circulos y una línea extra que no va)

492 Furthermore, Figure 12 suggest that highest amplitude cEOF2 years tend
 493 to coincide with strong ENSO years. The correlation between the absolute
 494 magnitude of the ONI and the magnitude of the cEOF2 is 0.45 (CI: 0.17
 495 – 0.67). This relationship, however, appears to be driven only by the three
 496 years with strongest ENSO events in the period (2015, 1997, and 1982) which
 497 also coincide with the three years with strongest cEOF2 magnitude. If those
 498 years are removed, the correlation becomes non-significant (0.047 (CI: -0.28 –
 499 0.36)). Furthermore, even when using all the datapoints, the Spearman corre-
 500 lation –which is robust to outliers– is also non-significant (0.2, p-value= 0.21).
 501 Therefore, the relationship between the magnitude of the cEOF2 train wave
 502 and ONI remains uncertain.

503 It could be concluded that the wave train represented by cEOF2 can be
 504 both part of the internal variability of the extratropical atmosphere or forced
 505 by tropical SSTs. In the former case, the wave train has little phase preference.
 506 However, when cEOF2 is excited by tropical SST variability, it tends to remain
 507 locked to the imaginary phase. This explains the relative overabundance of
 508 years with cEOF2 near positive and negative imaginary phase in Figure 7.

509 Figure 13 shows SST and streamfunction regression maps for cEOF1. Un-
 510 like the cEOF2 case, there is no significant pattern of SST anomalies associ-
 511 ated with either the Real or Imaginary cEOF1. Consistently, streamfunction

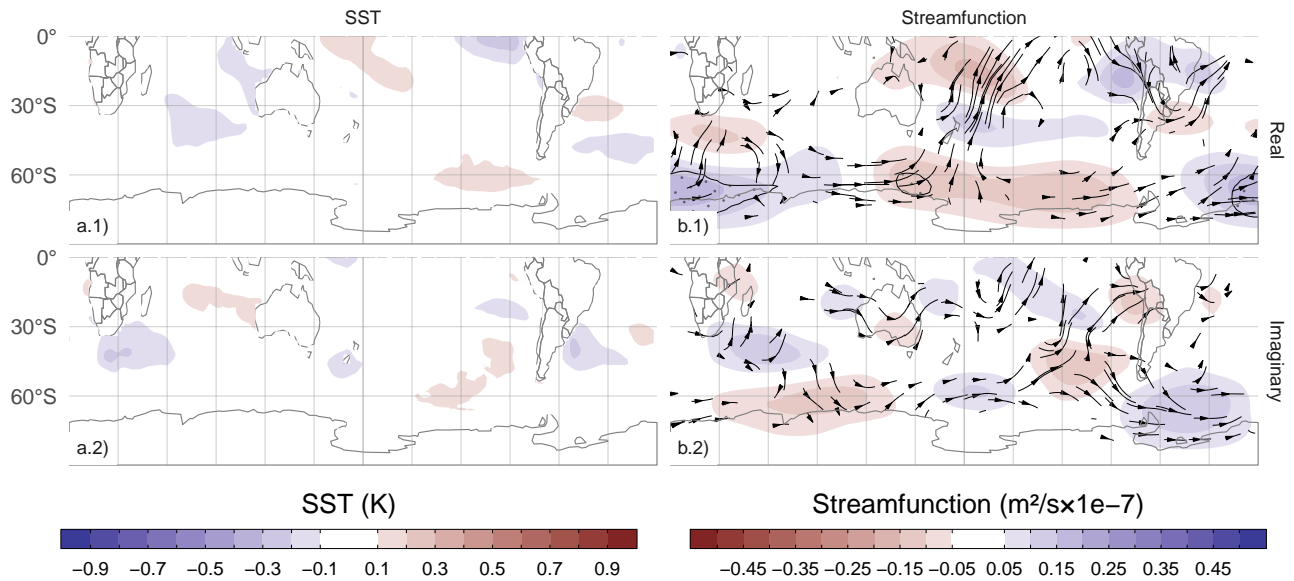


Fig. 13: Same as Figure 11 but for cEOF1. fig:sst-psi-1

512 anomalies do not show any tropical influence. Instead, the real and Imaginary
 513 cEOF1 are associated with zonally wave activity fluxes in the extra-tropics
 514 around 60°S, except for an equatorward flow from the coast of Antarctica
 515 around 150°E in the real component. This suggests that it's variability is
 516 driven primary by the internal variability of the extra-tropics.

517 Fig. 13 Tene en cuenta los mismos comentarios que en el figura 11 y revisa
 518 también la barra de colores para SST que quedo rara

519 3.5 Precipitation

520 The influence of cEOFs variability in continental rainfall of extra-tropical
 521 Southern Hemisphere is also explored. We focus on South America and Oceania
 522 sectors because there are no relevant signals in southern Africa (not shown).

523 Revisa el caption de la figura 14 que quedo un estilo distinto que los
 524 anteriores. Te falto aclarar tambien qué es la caja (¿la inventaste vos o habías
 525 utilizado la de algún otro trabajo?). Fijate tambien de aumentar la separación
 526 entre la columna izquierda y derecha para que no se superpongan los labels.
 527 Tambien fijate que esta barra de colores no te quedo con el borde externo como
 528 el resto.

529 The precipitation anomalies in Oceania associated with cEOF1 are weak
 530 and not statistically significant (Figure 14 column a) whereas cEOF2 is associ-
 531 ated with large and widespread anomalies. The Real cEOF2 is associated with
 532 positive seasonal anomalies in Northern and Eastern Australia, and negative

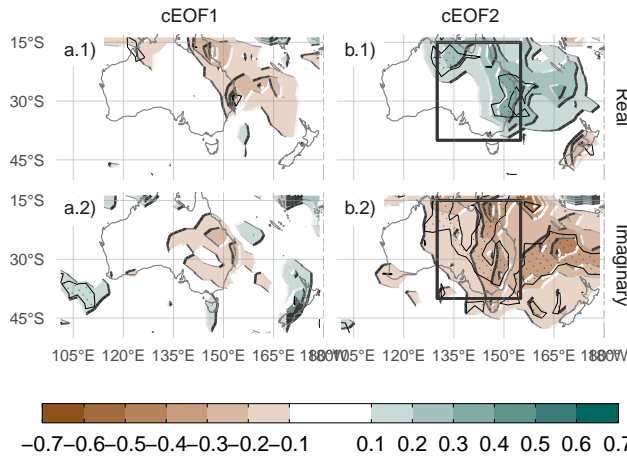


fig:pp-oceania
Fig. 14: Regression of SON mean precipitation anomalies in Oceania (mm per day, shaded) and (column a) cEOF1 the (row 1) Imaginary and (column 1) Real phase. For the 1979 – 2019. Areas marked with dots have p-values smaller than 0.05 adjusted for False Detection Rate. In black is the West Australia region, defined as the box between 130°E and 155°E and 40°S and 15°S.

533 ones over New Zealand, while precipitation anomalies associated with Imaginary
 534 cEOF2 are negative over all Eastern Australia. As it could be expected,
 535 these negative anomalies are similar to the springtime precipitation anomalies
 536 observed in relation with the Asymmetric SAM (Campitelli et al, 2021) and
 537 ENSO (Cai et al, 2011). **Acá te faltaría sacar un poco más el jugo asociando
 538 con la figura 11. Además, ¿revisaste si podes también usar algún resultado
 539 asociado a los PSA?**

540 **Revisa lo mismo que para la otra figura del tipo.**

541 To better understand the relationship between precipitation anomalies over
 542 Eastern Australia and the cEOF2, Figure 15 plots precipitation anomalies av-
 543 eraged over Eastern Australia (box in Figure 14) as a function of cEOF2 phase.
 544 The black line shows a sinusoidal fit, whose coefficients are fitted by weighted
 545 least squares using the magnitude of the EFO2 as weight. The r^2 correspond-
 546 ing to the fit is 0.41 (p-value < 0.001). There is a strong relationship between
 547 the phase of the cEOF2 and precipitation anomalies in Eastern Australia, but
 548 the Real and Imaginary phases we chose are not exactly aligned with the direc-
 549 tion that maximises this relationship. To perform a more in-depth analysis of
 550 the relationship between this pattern and precipitation in this region, it would
 551 be recommended to align one of the axis (either the Real or the Imaginary)
 552 to the phase that maximises the described relationship.

553 Figure 16 shows regression maps of seasonal precipitation with each cEOF
 554 in South America. cEOF1 is associated with negative regressions coefficients
 555 for precipitation in Southern Brazil and Paraguay, although these are not
 556 statistically significant (Fig. 16 column a). The strongest precipitation re-

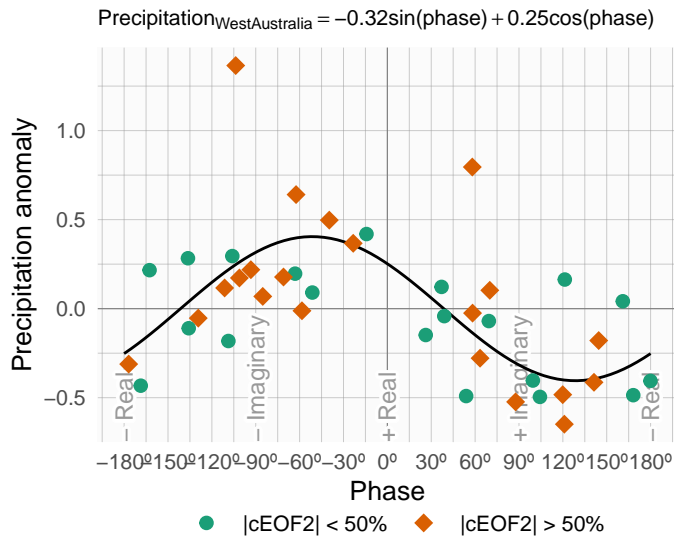


Fig. 15: Same as Figure 12 but for precipitation anomalies averaged between 130°E and 155°E and 40°S and 15°S (box shown in Figure 14 column b) in $\frac{\text{mm}}{\text{day}}$. Black line is the fit precipitation $\sim \sin(\text{phase}) + \cos(\text{phase})$ computed by weighted OLS using the magnitude of the cEOF2 as weights.

gression coefficients are the ones associated with the Imaginary cEOF2. The positive regression coefficients on Southeastern South America (SESA) and Central Chile, and negative ones over South Atlantic Convergence Zone is a well-known springtime precipitation signature of ENSO (Cai et al, 2020) and it is also similar to the precipitation anomalies associated with the A-SAM (Campitelli et al, 2021). **Lo mismo que te puse antes. Te faltaría sacar un poco más el jugo asociando con la figura 11. Además, ¿revisaste si puedes también usar algún resultado asociado a los PSA?**

This is not surprising considering the close relationship between the ONI, the A-SAM index and the Imaginary cEOF2 shown previously, but further consolidates the identification of this mode with the PSA pattern. On the other hand, the Real cEOF2 is associated with negative precipitation anomalies in a smaller area of SESA. Resembling the relationship between ONI and the phase of cEOF2 (Fig. 12), there is a cEOF2 phase dependence of the precipitation anomalies in SESA (not shown). These variables could be related wth a significant sinusoidal fit that has a statistically significant coefficient of determination of 0.27.

574 4 Conclusions

In this study we assessed the Austral Spring Extratropical Southern Hemisphere zonally assymetric circulation. For this purpose, two complex indices

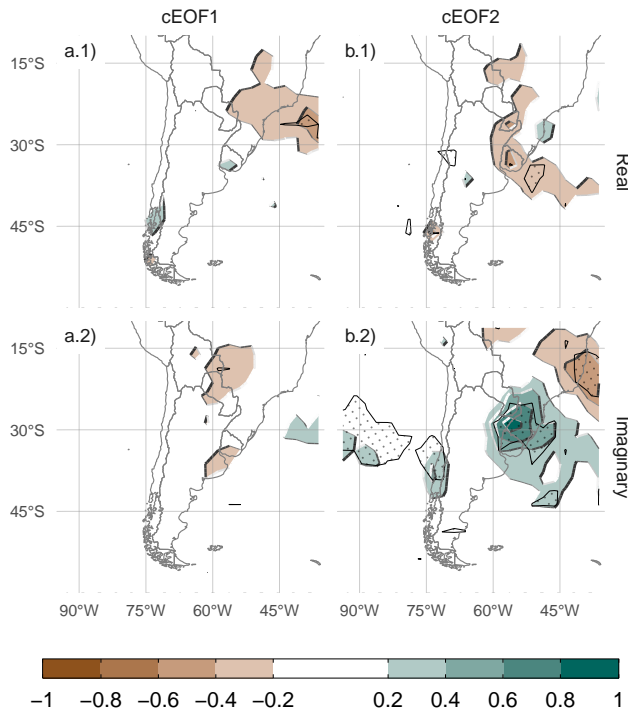


Fig. 16: As [fig:pp-america](#) but for South America

were derived using Complex Empirical Orthogonal Functions. This allowed us to characterise both the amplitude and phase of planetary waves that are not perfectly organised as sinusoidal waves with constant amplitude at each latitude circle.

The first complex EOF represents the variability of the zonal wave 1 in the stratosphere, but represents a more zonally symmetric monopole in the troposphere. There is a statistically positive trend in the magnitude of this cEOF, which is consistent with previous studies that showed secular changes in springtime wave-1-like patterns (e.g. Raphael, 2003). This mode is closely related to stratospheric variability such as anomalies in Total Ozone Column. Otherwise, this complex EOF is not related with SST variability and continental precipitation in the Southern Hemisphere.

The second complex EOF represents a wave-3 pattern with maximum magnitude in the Pacific sector. Essentially, it is an alternate representation of the PSA1 and PSA2 patterns (Mo and Paegle, 2001). We show that the Imaginary cEOF2 can be identified with the PSA1 and the Real cEOF2 with the PSA2. This cEOF prefers a phase aligned with the Imaginary cEOF2, because when ENSO is active, it forces the cEOF2 to be in the Imaginary phase. When ENSO is neutral, the cEOF2 is still active, but with no particular preferred phase. This mirrors the results of Cai and Watterson (2002), who showed that

597 the CSIRO Model can create PSA-like variability even in the absence of ENSO
598 forcing (with a climatological run), but the variability of one of the PSA modes
599 was enhanced when adding the ENSO signal. The magnitude of the cEOF2
600 appears not to be related to the magnitude of ENSO, except from the three
601 strongest ENSO events in the period which coincide with the three strongest
602 cEOF2 years.

603 We further show that the Imaginary cEOF2 is closely related to the South-
604 ern Annular Mode in the troposphere. In fact, it has a very close resemblance
605 to the zonally asymmetric portion of the SAM. This raises the possibility that
606 the asymmetric component of the SAM is actually a statistical contamination
607 of the PSA mode.

608 Precipitation anomalies in South America associated with the Imaginary
609 cEOF2 show a clear ENSO-like impact, with positive anomalies in South-
610 Eastern South America, negative anomalies in Southern Brazil and positive
611 anomalies in central Chile. Precipitation anomalies associated with the Real
612 cEOF2 are low and not statistically significant, showing that the Imaginary
613 phase is optimally aligned with the direction of maximum precipitation im-
614 pacts.

615 On the other hand, over Australia, both the Real and Imaginary phase are
616 associated with significant precipitation anomalies, and we further show that
617 the direction of maximum impact is not aligned with our chosen rotation of
618 cEOF2. However, this underscores the benefit of using complex EOF, since it
619 would be trivial to rotate it. *creo que esta idea convendría desarrollarla mejor*
620 *para el que no lo tenga tan claro*

621 To the extent that the cEOF2 can be identified with the PSA, what is the
622 advantage of the technique proposed here? The spatial fields that the cEOF2
623 index describes are in quadrature by construction, which makes it possible to
624 derive a proper amplitude and phase. Furthermore, because of the way they
625 are constructed, they are not forced to be orthogonal to the SAM. This makes
626 it possible to study their relationship with the SAM free of the statistical
627 contamination that comes with the usual definition of the PSA as the second
628 and third EOFs.

629 Further work should extend this analysis to other seasons and further study
630 the relationship between the cEOF2 and the SAM. In particular, it is not
631 clear whether the close identification between the Imaginary cEOF2 and the
632 Asymmetric SAM arises from physical processes or statistical contamination.

633 Code availability

code-availability

634 A version-controlled repository of the code used to create this analysis, includ-
635 ing the code used to download the data can be found at <https://github.com/>
636 eliocamp/shceof.

637 **5 References**

references

638 **References**

- 639 Adams JC, Swartztrauber PN, Sweet R (1999) FISHPACK, a package of Fortran
640 subprograms for the solution of separable elliptic partial differential
641 equations. <https://www2.cisl.ucar.edu/resources/legacy/fishpack>
- 642 Albers S, Campitelli E (2020) Rsoi: Import Various Northern and Southern
643 Hemisphere Climate Indices
- 644 Allaire JJ, Xie [aut Y, cre, McPherson J, Luraschi J, Ushey K, Atkins A, Wick-
645 ham H, Cheng J, Chang W, Iannone R, Dunning A, filter] AYNsL, Schloerke
646 B, Dervieux C, Aust F, Allen J, Seo J, Barrett M, Hyndman R, Lesur R,
647 Storey R, Arslan R, Oller S, RStudio, PBC, library) jFj, library; authors
648 listed in inst/rmd/h/jquery-AUTHORStxt) jcj, library; authors listed in
649 inst/rmd/h/jqueryui-AUTHORStxt) jUcjU, library) MOB, library) JTB,
650 library) BcB, Twitter, library) IB, library) AFh, js library) SJR, js library)
651 ISh, library) GFt, templates) JMP, Google, library) Ii, library) DRs, li-
652 brary) Ws, Gandy (Font-Awesome) D, Sperry (Ionicons) B, (Ionicons) D,
653 StickyTabs) ALj, filter) BPJpL, filter) AKpL (2020) Rmarkdown: Dynamic
654 Documents for R
- 655 Baldwin MP, Thompson DWJ (2009) A critical comparison of stratosphere–
656 troposphere coupling indices. Quarterly Journal of the Royal Meteorological
657 Society 135(644):1661–1672, DOI 10.1002/qj.479
- 658 Bamston AG, Chelliah M, Goldenberg SB (1997) Documentation of a
659 highly ENSO-related sst region in the equatorial pacific: Research note.
660 Atmosphere-Ocean 35(3):367–383, DOI 10.1080/07055900.1997.9649597
- 661 Bell B, Hersbach H, Berrisford P, Dahlgren P, Horányi A, Muñoz Sabater
662 J, Nicolas J, Radu R, Schepers D, Simmons A, Soci C, Thépaut
663 JN (2020) ERA5 monthly averaged data on pressure levels from
664 1950 to 1978 (preliminary version). Copernicus Climate Change Ser-
665 vice (C3S) Climate Data Store (CDS) (Accessed on <19-02-2021>),
666 <https://cds.climate.copernicus.eu/cdsapp#!/dataset/reanalysis-era5->
667 pressure-levels-monthly-means-preliminary-back-extension?tab=overview
- 668 Benjamini Y, Hochberg Y (1995) Controlling the False Discovery Rate: A
669 Practical and Powerful Approach to Multiple Testing. Journal of the Royal
670 Statistical Society: Series B (Methodological) 57(1):289–300, DOI 10.1111/
671 j.2517-6161.1995.tb02031.x
- 672 Cai W, Watterson IG (2002) Modes of Interannual Variability of the South-
673 ern Hemisphere Circulation Simulated by the CSIRO Climate Model. Jour-
674 nal of Climate 15(10):1159–1174, DOI 10.1175/1520-0442(2002)015<1159:
675 MOIVOT>2.0.CO;2
- 676 Cai W, van Rensch P, Cowan T, Hendon HH (2011) Teleconnection Pathways
677 of ENSO and the IOD and the Mechanisms for Impacts on Australian Rain-
678 fall. Journal of Climate 24(15):3910–3923, DOI 10.1175/2011JCLI4129.1
- 679 Cai W, McPhaden MJ, Grimm AM, Rodrigues RR, Taschetto AS, Garreaud
680 RD, Dewitte B, Poveda G, Ham YG, Santoso A, Ng B, Anderson W, Wang

- 681 G, Geng T, Jo HS, Marengo JA, Alves LM, Osman M, Li S, Wu L, Karam-
682 peridou C, Takahashi K, Vera C (2020) Climate impacts of the El Niño–
683 Southern Oscillation on South America. *Nature Reviews Earth & Environ-*
684 *ment* 1(4):215–231, DOI 10.1038/s43017-020-0040-3
- 685 Campitelli E (2020) metR: Tools for Easier Analysis of Meteorological Fields
686 Campitelli E, Díaz LB, Vera C (2021) Assessment of zonally symmetric and
687 asymmetric components of the Southern Annular Mode using a novel ap-
688 proach. *Clim Dyn* DOI 10.1007/s00382-021-05896-5
- 689 Dowle M, Srinivasan A (2020) Data.table: Extension of 'data.frame'
690 Fogt RL, Marshall GJ (2020) The Southern Annular Mode: Variability, trends,
691 and climate impacts across the Southern Hemisphere. *WIREs Climate*
692 *Change* 11(4):e652, DOI 10.1002/wcc.652
- 693 Gong D, Wang S (1999) Definition of Antarctic Oscillation index. *Geophysical*
694 *Research Letters* 26(4):459–462, DOI 10.1029/1999GL900003
- 695 Grytsai A (2011) Planetary wave peculiarities in Antarctic ozone distribution
696 during 1979–2008. *International Journal of Remote Sensing* 32(11):3139–
697 3151, DOI 10.1080/01431161.2010.541518
- 698 Hartmann DL, Garcia RR (1979) A Mechanistic Model of Ozone Transport
699 by Planetary Waves in the Stratosphere. *Journal of the Atmospheric Sci-*
700 *ences* 36(2):350–364, DOI 10.1175/1520-0469(1979)036<0350:AMMOOT>
701 2.0.CO;2
- 702 Hersbach H, Bell B, Berrisford P, Biavati G, Horányi A, Muñoz Sabater J,
703 Nicolas J, Peubey C, Radu R, Rozum I, Schepers D, Simmons A, Soci C, Dee
704 D, Thépaut JN (2019) ERA5 monthly averaged data on pressure levels from
705 1979 to present. Copernicus Climate Change Service (C3S) Climate Data
706 Store (CDS) (Accessed on <08-03-2021>), DOI 10.24381/cds.6860a573
- 707 Hobbs WR, Raphael MN (2010) Characterizing the zonally asymmetric com-
708 ponent of the SH circulation. *Clim Dyn* 35(5):859–873, DOI 10.1007/s00382-
709 009-0663-z
- 710 Horel JD (1984) Complex Principal Component Analysis: Theory and Exam-
711 ples. *Journal of Applied Meteorology and Climatology* 23(12):1660–1673,
712 DOI 10.1175/1520-0450(1984)023<1660:CPCATA>2.0.CO;2
- 713 Huang B, Thorne PW, Banzon VF, Boyer T, Chepurin G, Lawrimore JH,
714 Menne MJ, Smith TM, Vose RS, Zhang HM (2017) Extended Reconstructed
715 Sea Surface Temperature, Version 5 (ERSSTv5): Upgrades, Validations, and
716 Intercomparisons. *Journal of Climate* 30(20):8179–8205, DOI 10.1175/JCLI-
717 D-16-0836.1
- 718 Hufkens K (2020) Ecmwf: Programmatic interface to the two European Cen-
719 tre for Medium-Range Weather Forecasts API services
- 720 Irving D, Simmonds I (2015) A Novel Approach to Diagnosing Southern
721 Hemisphere Planetary Wave Activity and Its Influence on Regional Climate
722 Variability. *Journal of Climate* 28(23):9041–9057, DOI 10.1175/JCLI-D-15-
723 0287.1
- 724 Irving D, Simmonds I (2016) A New Method for Identifying the Pacific–South
725 American Pattern and Its Influence on Regional Climate Variability. *Journal*
726 *of Climate* 29(17):6109–6125, DOI 10.1175/JCLI-D-15-0843.1

- 727 Katz RW, Brown BG (1991) The problem of multiplicity in research on
728 teleconnections. International Journal of Climatology 11(5):505–513, DOI
729 10.1002/joc.3370110504
- 730 Marshall GJ (2003) Trends in the Southern Annular Mode from Observations
731 and Reanalyses. J Climate 16(24):4134–4143, DOI 10.1175/1520-0442(2003)
732 016<4134:TITSAM>2.0.CO;2
- 733 Mo KC (2000) Relationships between Low-Frequency Variability in the South-
734 ern Hemisphere and Sea Surface Temperature Anomalies. Journal of Cli-
735 mate 13(20):3599–3610, DOI 10.1175/1520-0442(2000)013<3599:RBLFVI>
736 2.0.CO;2
- 737 Mo KC, Paegle JN (2001) The Pacific–South American modes and their down-
738 stream effects. International Journal of Climatology 21(10):1211–1229, DOI
739 10.1002/joc.685
- 740 Plumb RA (1985) On the Three-Dimensional Propagation of Stationary
741 Waves. J Atmos Sci 42(3):217–229, DOI 10.1175/1520-0469(1985)042<0217:
742 OTTDPO>2.0.CO;2
- 743 R Core Team (2020) R: A Language and Environment for Statistical Comput-
744 ing. R Foundation for Statistical Computing, Vienna, Austria
- 745 Raphael M (2003) Recent, Large-Scale Changes in the Extratropical Southern
746 Hemisphere Atmospheric Circulation. J Climate 16(17):2915–2924, DOI
747 10.1175/1520-0442(2003)016<2915:RLCITE>2.0.CO;2
- 748 Raphael MN (2004) A zonal wave 3 index for the Southern Hemisphere. Geo-
749 physical Research Letters 31(23), DOI 10.1029/2004GL020365
- 750 Raphael MN (2007) The influence of atmospheric zonal wave three on
751 Antarctic sea ice variability. Journal of Geophysical Research: Atmospheres
752 112(D12), DOI 10.1029/2006JD007852
- 753 Smith AK (1995) Numerical simulation of global variations of temperature,
754 ozone, and trace species in the stratosphere. Journal of Geophysical Re-
755 search: Atmospheres 100(D1):1253–1269, DOI 10.1029/94JD02395
- 756 Trenberth KE (1980) Planetary Waves at 500 mb in the Southern Hemisphere.
757 Mon Wea Rev 108(9):1378–1389, DOI 10.1175/1520-0493(1980)108<1378:
758 PWAMIT>2.0.CO;2
- 759 Trenberth KF, Mo KC (1985) Blocking in the Southern Hemisphere. Mon Wea
760 Rev 113(1):3–21, DOI 10.1175/1520-0493(1985)113<0003:BITSH>2.0.CO;
761 2
- 762 Turner J, Hosking JS, Bracegirdle TJ, Phillips T, Marshall GJ (2017) Variabil-
763 ity and trends in the Southern Hemisphere high latitude, quasi-stationary
764 planetary waves. International Journal of Climatology 37(5):2325–2336,
765 DOI 10.1002/joc.4848
- 766 van Loon H, Jenne RL (1972) The zonal harmonic standing waves in the
767 southern hemisphere. Journal of Geophysical Research 77(6):992–1003, DOI
768 10.1029/JC077i006p00992
- 769 Walker SGT (1914) Correlation in Seasonal Variations of Weather, III: On the
770 Criterion for the Reality of Relationships Or Periodicities. Meteorological
771 Office

- 772 Wickham H (2009) Ggplot2: Elegant Graphics for Data Analysis. Use R!,
773 Springer-Verlag, New York, DOI 10.1007/978-0-387-98141-3
- 774 Wilks D (2011) Statistical Methods in the Atmospheric Sciences, vol 100.
775 Elsevier, DOI 10.1016/B978-0-12-385022-5.00022-1
- 776 Wilks DS (2016) “The Stippling Shows Statistically Significant Grid Points”:
777 How Research Results are Routinely Overstated and Overinterpreted, and
778 What to Do about It. Bull Amer Meteor Soc 97(12):2263–2273, DOI 10.
779 1175/BAMS-D-15-00267.1
- 780 Wirth V (1993) Quasi-stationary planetary waves in total ozone and their
781 correlation with lower stratospheric temperature. Journal of Geophysical
782 Research: Atmospheres 98(D5):8873–8882, DOI 10.1029/92JD02820
- 783 Xie P, Arkin PA (1997) Global Precipitation: A 17-Year Monthly Analysis
784 Based on Gauge Observations, Satellite Estimates, and Numerical Model
785 Outputs. Bull Amer Meteor Soc 78(11):2539–2558, DOI 10.1175/1520-
786 0477(1997)078<2539:GPAYMA>2.0.CO;2
- 787 Xie Y (2015) Dynamic Documents with R and Knitr, 2nd edn. Chapman and
788 Hall/CRC, Boca Raton, Florida